A pilot study using flying spot laser thermography and signal reconstruction

Optics and Lasers in Engineering 188 (2025) 108901

Contents lists available at ScienceDirect

Optics and Lasers in Engineering

journal homepage: www.elsevier.com/locate/optlaseng

A pilot study using flying spot laser thermography and signal reconstruction

Luca Santoro *, Raffaella Sesana

Politecnico di Torino, Corso Duca degli Abruzzi, 24, Turin, 10129, Italy

ARTICLE INFO

Dataset link: https://github.com/lucasantoro97/atpp, https://lucasantoro97.github.io/atpp/

Keywords:
Active thermography
Non-destructive testing
Flying spot laser thermography
Principal component analysis
Independent component analysis
Signal processing

ABSTRACT

Active thermography (AT) has emerged as a critical non-destructive testing and evaluation (NDT&E) technique for identifying subsurface defects in diverse industrial materials. Despite its widespread application, AT faces challenges such as inadequate heat input, noisy thermal signals, and non-uniform heating, which can obscure defect detection. This study introduces an enhanced approach leveraging flying spot laser thermography combined with advanced signal processing techniques to address these challenges. A meticulously designed calibration block, embedded with 180 spherical and rectangular notch defects of varying depths and dimensions, was fabricated using 3D printing to serve as the experimental model. The laser-induced thermal data were acquired at three distinct scanning speeds and underwent temporal alignment to synchronize heating events across all pixels. Principal Component Analysis (PCA) and Independent Component Analysis (ICA) were subsequently applied to the aligned datasets to extract and isolate defect-related thermal signatures. PCA effectively reduced data dimensionality and highlighted major thermal diffusion patterns associated with significant defects, particularly notched anomalies. However, its sensitivity diminished for smaller or deeper defects. In contrast, ICA provided a more refined separation of thermal signals, enhancing defect visualization and contrast, especially at slower scanning speeds where higher heat input improved thermal differentiation. Notably, ICA demonstrated superior performance in isolating notched defects compared to spherical ones due to pronounced thermal gradients. The findings underscore the potential of combining flying spot thermography with PCA and ICA to enhance defect detection and characterization in NDT&E applications. Future work will focus on optimizing scanning parameters through simulation models and integrating machine learning algorithms to further improve the detection of smaller and shallower defects, thereby advancing the precision and efficacy of thermal analysis techniques.

1. Introduction

Active thermography (AT) has evolved into a pivotal non-destructive testing and evaluation (NDT&E) modality for detecting subsurface defects in diverse industrial materials [1–10]. Various approaches, such as pulsed thermography (PT) and lock-in thermography (LT), have gained acceptance for their capacity to identify damage or flaws in both metallic and composite components [11–14]. Nonetheless, challenges related to inadequate heat input, noisy thermal signals, and non-uniform heating can obscure subsurface details [15–19], prompting the development of improved excitation schemes and robust post-processing algorithms [20,21].

In the context of non-stationary thermal wave imaging, modulated thermal excitations have been demonstrated to enhance the sensitivity and resolution of thermographic inspections [22,23]. Barker-coded thermal wave imaging (BCTWI) and frequency-modulated thermal wave imaging (FMTWI) exemplify the efficacy of non-stationary excitations, where pulse-compression principles are often applied to maximize defect detection [24,25]. Coupling these excitation strategies with advanced signal processing methods further boosts defect visibility by isolating defect-related thermal contrasts from background noise [26–29].

Recent literature showcases the adoption of blind source separation techniques (i.e., principal component analysis (PCA) and independent component analysis (ICA)) for defect detection in thermography data [30,31]. For example, PCA can reduce dimensionality and highlight

* Corresponding author.
E-mail address: luca.santoro@polito.it (L. Santoro).
URL: https://lucasantoro97.github.io/cv/ (L. Santoro).

https://doi.org/10.1016/j.optlaseng.2025.108901
Received 15 January 2025; Received in revised form 10 February 2025; Accepted 19 February 2025

Table 1
List of symbols and their definitions.

Symbol	Definition
$d_{i,j}$	Depth of defect at grid position (i, j).
$d_{\min}$	Minimum defect depth.
$d_{\max}$	Maximum defect depth.
$l_{i,j}$	Lateral dimension of defect at grid position (i, j).
$l_{\min}$	Minimum lateral dimension.
$l_{\max}$	Maximum lateral dimension.
ρ	Density.
κ	Thermal conductivity.
ρ_0	Baseline density of PLA.
κ_0	Baseline thermal conductivity of PLA.
$\Delta\rho_{i,j}$	Perturbation in density due to defect $D_{i,j}$.
$\Delta\kappa_{i,j}$	Perturbation in thermal conductivity due to defect $D_{i,j}$.
v_j	Scanning speed for the j-th test ($v_1 = 60$ mm/s, $v_2 = 120$ mm/s, $v_3 = 360$ mm/s).
ℓ	Length of the scan.
t_j	Time taken to complete the scan at speed v_j.
$T(p, t; v_j)$	Temperature at pixel p and time t for scanning speed v_j.
$T_{\text{undersampled}}(p, t_k; v_j)$	Undersampled temperature data.
$T_{\text{aligned}}(p, t)$	Temporally aligned temperature data.
Δt	Temporal resolution of the reconstructed signals.
K	Total number of synchronized time frames.
M	Total number of pixels ($M = H \times W$).
$\mathbf{X}$	Data matrix.
$\mathbf{X}_{\text{centered}}$	Centered data matrix.
μ	Mean vector.
$\mathbf{C}$	Covariance matrix.
$\mathbf{u}_i$	Eigenvectors (principal components).
λ_i	Eigenvalues.
$\mathbf{U}_L$	Matrix of top L eigenvectors.
$\mathbf{Y}$	Reduced-dimensional representation.
$\mathbf{X}_{\text{reconstr}}$	Reconstructed data matrix.
$\mathbf{A}$	Mixing matrix.
$\mathbf{S}$	Source signals (independent components).
$\mathbf{W}$	Unmixing matrix.
$p(\mathbf{S})$	Joint probability distribution of source signals.
$\mathcal{F}$	Contrast function.
$g(\cdot)$	Non-linear function (e.g., tanh).
H	Entropy function.
τ_p	Time offset for pixel p.
$\mathbf{S}$	Shift matrix encoding τ_p.
$\mathbf{w}_i$	Row of the unmixing matrix $\mathbf{W}$.
$*$	Temporal shift operator.
t_p^{peak}	Time of peak temperature for pixel p.
t_{ref}	Reference peak time.

subsurface anomalies by extracting orthogonal components [32,33], whereas ICA decouples superimposed signals to unearth more subtle flaw-related features [34,35]. Subsequent enhancements, including tensor decomposition and total variation regularization, have been reported to improve defect contrast and reduce spurious signals [36,37].

Defect sizing, depth profiling, and signal-to-noise ratio (SNR) optimization remain crucial focal points in active thermography research [38,39]. Thermographic signal reconstruction (TSR) and other curve-fitting or wavelet-based methods have been shown to mitigate non-uniform heating effects and amplify defect signatures [40,41], thereby enabling robust detection in metals, composites, and even polymeric materials [42,43]. Likewise, hybrid approaches merging phase, amplitude, or reconstructed data can markedly improve defect characterization [44,45].

Carbon fiber-reinforced polymer (CFRP) structures, in particular, have garnered substantial attention due to their vulnerability to delamination or impact-induced damage [46,47]. Eddy current pulsed thermography (ECPT) further extends thermographic capabilities by inducing localized heating through eddy currents, thus revealing microcracks, delaminations, or other flaws [48–50]. Moreover, spatial-transient pattern analysis and optical flow-based algorithms have been successfully applied to ECPT data to detect subtle or deep defects in CFRP and metallic parts [51,52].

In addition to conventional pulse or lock-in-based inspections, multi-frequency and coded excitations have recently been investigated, improving depth resolution and reducing peak power requirements [53,54]. These methods align closely with advanced feature extraction schemes, such as sparse PCA or robust tensor decomposition, to filter noise and highlight defect signatures in highly cluttered data [55,56]. Regardless of the excitation strategy, the combined use of PCA, ICA, or other dimensionality-reduction methods remains essential to extract meaningful features for reliable NDT&E [57,58].

Laser thermography, another AT variant, exploits localized or scanning laser beams for heating, enabling improved detection of near-surface cracks or delaminations [59,60]. Additionally, coded-laser scanning or pulse-compression approaches stand out for their high inspection throughput and increased SNR, particularly when focusing on inner damage [61,62]. Furthermore, the limitations of existing AT methods—including non-uniform heating and high noise levels—motivate the development of this new flying spot laser thermography technique. Such approaches, when augmented by advanced machine learning frameworks (e.g., convolutional autoencoders), allow for robust defect detection and enhanced visualization of subtle damage [63,64].

Multiple studies have shown that defect information in thermographic data can be effectively separated into background, noise, and meaningful thermal features by employing local sparseness and image fusion approaches [65,66], thus improving the interpretability of the results and reducing misclassification [67,68]. Moreover, two-phased fusion criteria and physical-meaningful constraints have been integrated

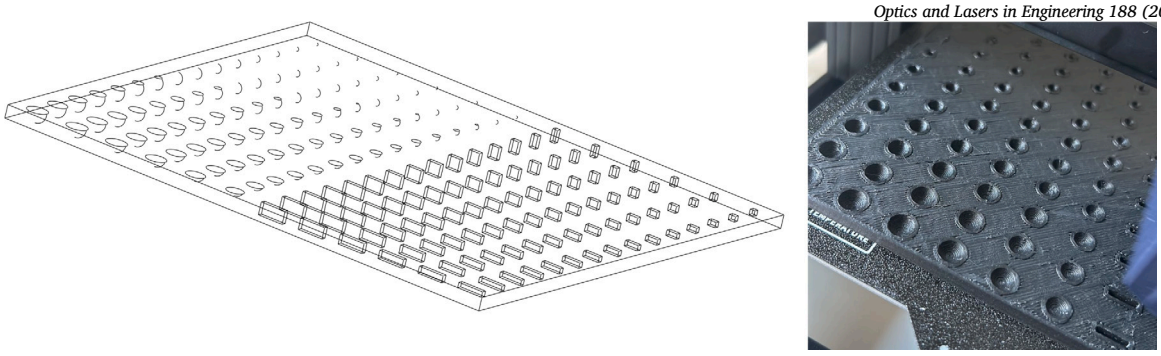

(a) 3D view of calibration block

(b) Calibration Block during manufacturing process

Fig. 1. Calibration block.

to preserve subtle features while attenuating coil or lens artifacts in ECPT [1,69].

When it comes to crack-depth estimation and defect-characterization, recently proposed feature extraction strategies combine maximum thermal response, crossing point of impulse responses, and skewness computations to achieve higher accuracies [2,11]. Wavelet processing, partial least-squares regression, or polynomial approximation can also further refine the fault quantification, offering significantly improved contrast-to-noise metrics and detection rates [12,15]. In the study of advanced composites, including CFRP and basalt-carbon hybrids, the synergy of coded excitations and principal component thermography (PCT) has demonstrated excellent results for intralaminar and interlaminar damage assessment [16,20].

Algorithmic enhancements via robust principal component analysis (RPCA) or independent structural image extraction approaches also suggest that physical effect identification can mitigate optical or thermal perturbations [21,22]. Indeed, leveraging spatio-temporal continuity constraints, morphological analysis, or spatial coherence measures further improves the final defect maps [23,24]. Therefore, the combination of an effective excitation scheme, intelligent signal processing, and domain-specific knowledge remains a cornerstone of modern active thermographic research [25,26].

Within this rapidly growing domain, flying spot thermography, which employs a localized moving heat source, holds promise for enhancing heat input control and spatial resolution, especially for open-crack detection in metallic or composite structures [27,30]. Although such scanning methods can produce large datasets under complex thermal diffusion conditions, they also facilitate customizable heating profiles suited for different material properties [31,32]. The improved control over localized heating helps to isolate defects from background or surface reflectivity variations [33,34].

Building upon these advancements, the objective of this paper is to exploit flying spot thermography to refine heat input control during active thermographic inspections and thereby improve defect characterization. The method reconstructs a signal comparable to that of pulsed thermography, thus enabling the application of standard data analysis techniques such as PCA and ICA.

2. Materials and methods

The present study aims to validate a signal reconstruction methodology for flying spot laser thermography through the utilization of a meticulously designed calibration block. The nomenclature is presented in Table 1. The calibration block, as depicted in Fig. 1a, is a parallelepiped with dimensions of 200 mm × 200 mm × 5 mm. Embedded within this block are 180 hidden defects, systematically distributed to facilitate comprehensive testing of the proposed methodology. These defects are divided into two categories: spherical-shaped and rectangular notch, with each category constituting half of the total defect population.

Table 2
Specifications of embedded defects in the calibration block.

Defect Type	Dimension	Range	Units
Spherical Defects	Diameter	0.5 – 4	mm
	Depth	0.2 – 3	mm
Rectangular Notches	Length	2 – 10	mm
	Depth	0.2 – 3	mm

The defects are organized in a 6×15 grid pattern, ensuring controlled variation in both depth and dimension. Specifically, along the six rows, the depth of the defects varies from 0.2 mm to 3 mm, while along the fifteen columns, the lateral dimensions are systematically varied. For the spherical defects, the diameter ranges from 0.5 mm to 4 mm, whereas the rectangular notch defects maintain a constant width of 2 mm with lengths varying from 2 mm to 10 mm. These specifications are summarized in Table 2.

Mathematically, the spatial arrangement of defects within the block can be described using a two-dimensional grid coordinate system. Let (i, j) denote the position of a defect in the i-th row and j-th column of the grid, where $i = 1, \ldots, 6$ and $j = 1, \ldots, 15$. For each defect, its depth $d_{i,j}$ and lateral dimension $l_{i,j}$ are defined based on its grid position, ensuring systematic variation along both axes. Specifically, the depth varies linearly across the rows, while the lateral dimensions vary across the columns according to the following relationships:

$$d_{i,j} = d_{\min} + \left(\frac{d_{\max} - d_{\min}}{6 - 1} \right) (i - 1), \tag{1}$$

$$l_{i,j} = l_{\min} + \left(\frac{l_{\max} - l_{\min}}{15 - 1} \right) (j - 1), \tag{2}$$

where $d_{\min}$ and $d_{\max}$ represent the minimum and maximum depths, respectively, and $l_{\min}$ and $l_{\max}$ denote the minimum and maximum lateral dimensions for each defect type.

The calibration block was fabricated using an AnyCubic Kobra 2 Neo 3D printer with polylactic acid (PLA) filament. Surface smoothing was achieved through controlled thermal treatment, where the block was subjected to a temperature of 60 °C for 10 minutes, allowing minor surface irregularities to be mitigated without altering the embedded defect geometries. In Fig. 1b an image of the calibration block during its manufacturing is presented; the hidden defects are visible since the image has been taken during manufacturing. With successive layers, the defects will be embedded in the bulk of the material.

Mathematically, the defects can be represented as perturbations in the otherwise uniform material properties of the PLA block. Let the baseline material properties be denoted by ρ (density) and κ (thermal

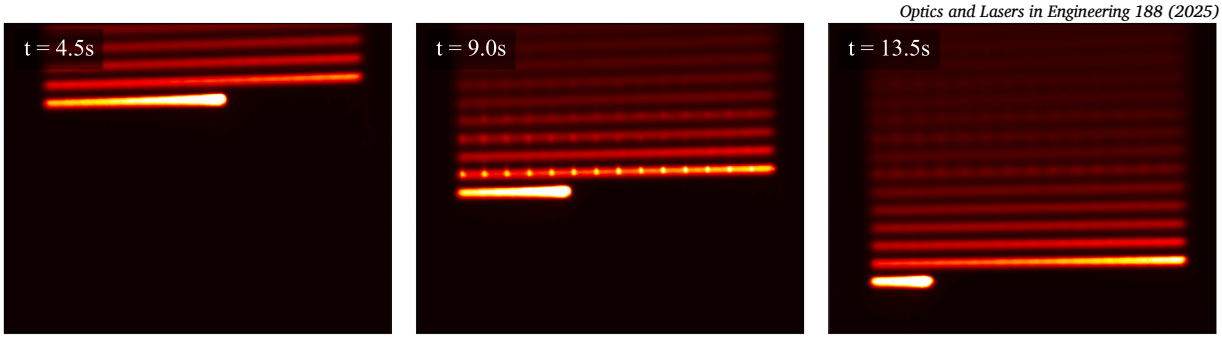

Fig. 2. Subsequent thermographic frames of flying spot laser scan.

conductivity). The presence of a defect $D_{i,j}$ introduces a localized variation in these properties, which can be modeled as:

$$\rho_{D_{i,j}} = \rho_0 + \Delta\rho_{i,j}, \tag{3}$$

$$\kappa_{D_{i,j}} = \kappa_0 + \Delta\kappa_{i,j}, \tag{4}$$

where ρ_0 and κ_0 are the baseline density and thermal conductivity of PLA, respectively, and $\Delta\rho_{i,j}$ and $\Delta\kappa_{i,j}$ represent the perturbations introduced by the defect $D_{i,j}$.

By systematically varying the depth and dimension of the defects, the study ensures that the signal reconstruction methodology is rigorously tested against a wide spectrum of defect-induced thermal anomalies.

2.1. Experimental setup

The calibration block underwent a horizontal laser scanning process at three distinct velocities, denoted by v_1, v_2, v_3, where $v_1 = 60mm/s$, $v_2 = 120mm/s$, $v_3 = 360mm/s$. The laser induces localized heating on the surface of the block, generating temporal temperature profiles across each pixel p of the scanned area (see Fig. 2). The scanning speed v_j influences both the temporal resolution and the thermal diffusion characteristics captured during the measurement. The relationship between scanning speed and thermal response can be modeled as:

$$v_j = \frac{\ell}{t_j}, \tag{5}$$

where ℓ is the length of the scan and t_j is the time taken to complete the scan at speed v_j.

The temperature data $T(p,t;v_j)$ was acquired using a thermal imaging system synchronized with the laser scanning head (Multi-DES), consisting in a FLIR A6751sc thermal camera and a pulsed laser from IPG Photonics. The FLIR camera is built around an advanced Indium Antimonide (InSb) detector offering a selectable spectral range of either 3–5 µm or 1–5 µm, and it captures thermal images at a resolution of 640×512 pixels with a detector pitch of 15 µm. With a noise-equivalent temperature difference (NETD) of less than 20 mK (typically 18 mK), the camera delivers exceptional thermal sensitivity and accuracy over a temperature range extending up to 1500 °C. Its 50 mm lens, combined with a highly flexible integration time ranging from 480 ns to 687 sec, allows for precise control over exposure conditions. Moreover, the camera offers a programmable full-window frame rate from as low as 0.0015 Hz up to 125 Hz, and it is capable of reaching a maximum frame rate of 4175 Hz (in a 16×4 window mode) within a robust 14-bit dynamic range.

Complementing the thermal imaging system is a pulsed laser manufactured by IPG Photonics (model YLPN-V2-1-100-50-50). Operating in pulsed mode, the laser delivers a maximum pulse energy of 1 mJ and a nominal average output power of 50 W. It features a nominal pulse repetition rate of 50 kHz with an adjustable repetition rate ranging from 2 kHz to 200 kHz, and emits pulses with a duration of 100 ns at a central wavelength of 1064 nm. The laser maintains a high beam quality with $M^2 < 2$.

For each scanning speed v_j, the temperature at each pixel p and time t is recorded, yielding a three-dimensional dataset $T \in \mathbb{R}^{H\times W\times F}$, where H and W denote the spatial dimensions (height and width) of the scanned area, and F represents the number of temporal frames captured during the scan. The data were acquired at 100 Hz frequency, however, to enhance computational efficiency and reduce data redundancy, temporal undersampling was performed by selecting every fifth frame:

$$T_{\text{undersampled}}(p,t_k;v_j) = T(p,t_{5k};v_j), \quad k = 1,2,\ldots,\left\lfloor \frac{F}{5} \right\rfloor. \tag{6}$$

This results in a reduced dataset $T' \in \mathbb{R}^{H\times W\times F'}$, where $F' = \left\lfloor \frac{F}{5} \right\rfloor$.

2.2. Temporal alignment of temperature signals

A critical step in the data analysis pipeline involves the temporal alignment of temperature signals across all pixels to ensure that the initiation and termination of heating events occur simultaneously. Let $T_p(t;v_j)$ denote the temperature profile of pixel p at time t for scanning speed v_j. The alignment process seeks to find a time offset τ_p for each pixel p such that:

$$T_p(t+\tau_p;v_j) = T_p^{\text{aligned}}(t), \tag{7}$$

where $T_p^{\text{aligned}}(t)$ represents the synchronized temperature profile.

To determine τ_p, the time of peak temperature t_p^{peak} for each pixel is identified:

$$t_p^{\text{peak}} = \arg\max_t T_p(t;v_j). \tag{8}$$

A reference peak time t_{ref} is established, typically chosen as the maximum of all t_p^{peak} across pixels:

$$t_{\text{ref}} = \max_p t_p^{\text{peak}}. \tag{9}$$

The time offset for each pixel is then calculated as:

$$\tau_p = t_{\text{ref}} - t_p^{\text{peak}}. \tag{10}$$

This ensures that the peak temperature events across all pixels are temporally aligned.

The aligned temperature data T_{aligned} is constructed by shifting each pixel's temperature profile according to its respective τ_p:

$$T_{\text{aligned}}(p,t) = T_p(t+\tau_p;v_j). \tag{11}$$

Mathematically, this can be represented as a translation operation in the temporal domain:

$$\mathbf{T}_{\text{aligned}} = \mathbf{T} * \mathbf{S}, \tag{12}$$

where $*$ denotes the temporal shift operator and $\mathbf{S}$ is a shift matrix encoding the τ_p values for each pixel.

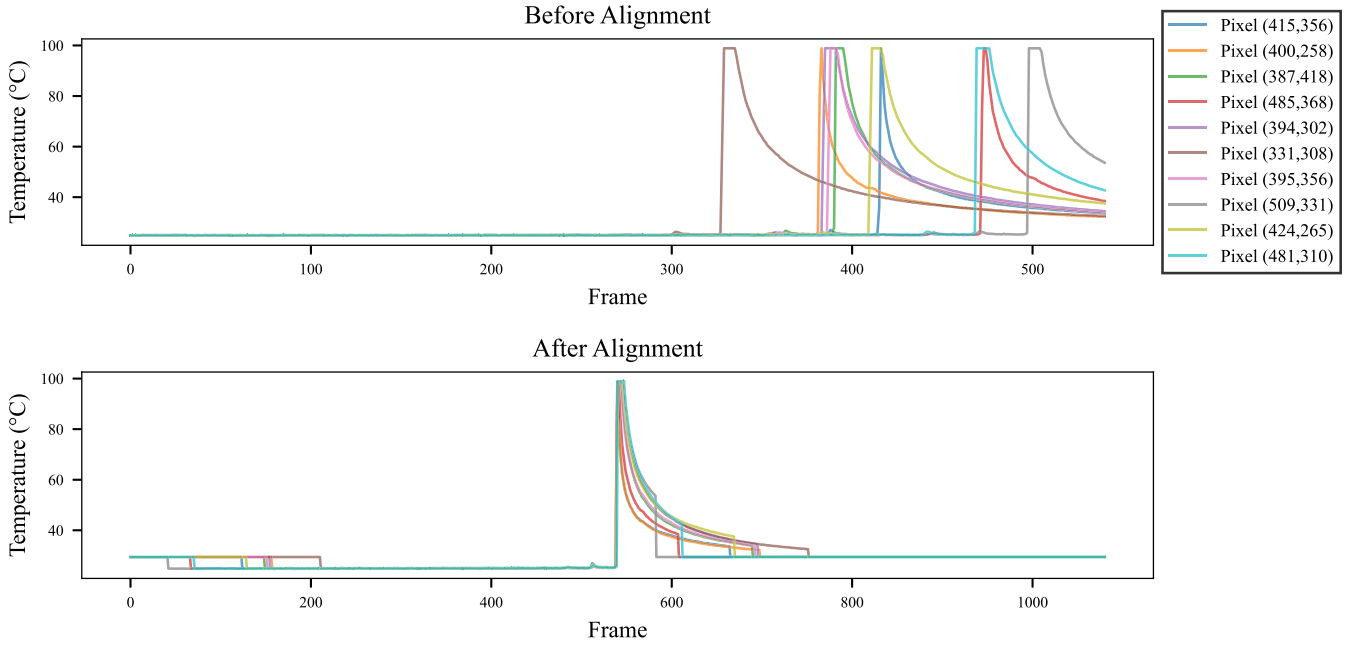

Fig. 3. Temperature profiles of selected pixels before and after temporal alignment for the v_1 dataset. The alignment ensures that the heating events across all pixels are temporally synchronized.

Fig. 3 presents the temperature profiles of selected pixels from the v_1 test dataset before and after temporal alignment. The alignment process successfully synchronized the heating onset and peak temperatures across all pixels, mitigating phase discrepancies induced by varying scanning speeds. The parameter of the laser and the camera calibration used in these tests were optimized for defect detection, however this led to signal saturation in the peak region since the heating temperature of the component exceeds the maximum temperature in the thermal camera calibration range, saturating the signal in the sensor.

Post-alignment, the temperature signals are reconstructed to ensure that the heating events across all pixels commence and conclude simultaneously. In fact, the temperature signal might start or finish at a different time instant between different pixels; to this aim, the average value of all the acquisition is substituted to padded frames as follow.

The reconstruction involves interpolating the shifted temperature profiles to a common temporal grid, thereby mitigating any residual temporal discrepancies introduced during the alignment process. Let Δt denote the temporal resolution of the reconstructed signals, and K the total number of synchronized time frames:

$$T_{\text{reconstr}}(p,k) = \frac{1}{\Delta t} \int_{k\Delta t}^{(k+1)\Delta t} T_{\text{aligned}}(p,t)\, dt. \tag{13}$$

This integral ensures that the reconstructed temperature at each pixel and time frame accurately represents the average temperature over the interval $[k\Delta t, (k+1)\Delta t)$.

The reconstructed data matrix $\mathbf{X} \in \mathbb{R}^{M\times K}$ is then formed, where $M = H \times W$ is the total number of pixels, and K is the number of synchronized time frames. Each row $\mathbf{x}_m$ of $\mathbf{X}$ corresponds to the temperature profile of pixel m:

$$\mathbf{x}_m = \begin{bmatrix} T_{\text{reconstr}}(m,1) & T_{\text{reconstr}}(m,2) & \cdots & T_{\text{reconstr}}(m,K) \end{bmatrix}. \tag{14}$$

2.3. Principal component analysis (PCA)

PCA is a fundamental statistical technique employed to reduce the dimensionality of a dataset $\mathbf{X} \in \mathbb{R}^{M\times K}$ while preserving as much variability as possible. The primary objective of PCA is to identify the principal modes of variation in the data, which facilitates the visualization and analysis of high-dimensional datasets by transforming them into a lower-dimensional space.

The process begins with data preprocessing, where the dataset $\mathbf{X}$ is centered by subtracting the mean of each variable to ensure that each feature has a zero mean. This centering is mathematically represented as:

$$\mathbf{X}_{\text{centered}} = \mathbf{X} - \mu, \quad \mu = \frac{1}{K}\sum_{k=1}^{K} \mathbf{x}_k, \tag{15}$$

where $\mathbf{x}_k$ denotes the k-th data sample. Centering the data is crucial as it ensures that PCA accurately identifies the directions of maximum variance without being biased by the mean of the data.

Following centering, the covariance matrix $\mathbf{C} \in \mathbb{R}^{M\times M}$ is computed to capture the pairwise covariance between variables:

$$\mathbf{C} = \frac{1}{K-1}\mathbf{X}_{\text{centered}}\mathbf{X}_{\text{centered}}^{\top}. \tag{16}$$

The covariance matrix provides a measure of how much each variable varies with every other variable, thereby encapsulating the internal structure of the data.

To identify the principal components, an eigen decomposition of the covariance matrix $\mathbf{C}$ is performed:

$$\mathbf{C}\mathbf{u}_i = \lambda_i \mathbf{u}_i, \quad i = 1, 2, \ldots, M, \tag{17}$$

where λ_i are the eigenvalues and $\mathbf{u}_i$ are the corresponding eigenvectors. The eigenvalues indicate the amount of variance captured by each principal component, while the eigenvectors determine the direction of these components in the feature space. The eigenvalues are typically ordered in descending order $\lambda_1 \geq \lambda_2 \geq \cdots \geq \lambda_M$, and due to the symmetric nature of $\mathbf{C}$, the eigenvectors are orthogonal.

To achieve dimensionality reduction, the top L eigenvectors corresponding to the largest eigenvalues are selected, forming the matrix $\mathbf{U}_L = [\mathbf{u}_1, \mathbf{u}_2, \ldots, \mathbf{u}_L] \in \mathbb{R}^{M\times L}$. The original data is then projected onto these principal components to obtain the reduced-dimensional representation $\mathbf{Y} \in \mathbb{R}^{L\times K}$:

$$\mathbf{Y} = \mathbf{U}_L^{\top}\mathbf{X}_{\text{centered}}. \tag{18}$$

This projection transforms the data into a new coordinate system where the axes (principal components) are ordered by the amount of variance they capture, effectively capturing the directions of maximum variance in the data.

The original data can be approximated by reconstructing it from the principal components using the selected eigenvectors:

$$\mathbf{X}_{\text{reconstr}} = \mathbf{U}_L \mathbf{Y} + \mu. \tag{19}$$

This reconstruction allows for an approximation of the original high-dimensional data using a lower-dimensional representation, facilitating tasks such as noise reduction and feature extraction.

The proportion of variance explained by each principal component is given by the explained variance ratio:

$$\text{Explained Variance Ratio} = \frac{\lambda_i}{\sum_{j=1}^{M} \lambda_j}, \quad i = 1, 2, \ldots, L. \tag{20}$$

This metric is instrumental in determining the number of principal components L to retain, ensuring that a sufficient amount of the data's variability is preserved while reducing dimensionality.

In summary, PCA transforms the original data into a new coordinate system where the axes are ordered by the amount of variance they capture. This transformation not only reduces dimensionality but also facilitates the identification of dominant patterns in the data, such as thermal diffusion modes associated with underlying defects.

2.4. Independent component analysis (ICA)

Independent Component Analysis (ICA) is an advanced computational method designed to separate a multivariate signal into additive, statistically independent non-Gaussian components. Unlike PCA, which focuses on uncorrelated components, ICA aims to identify components that are not only uncorrelated but also statistically independent, making it a powerful tool for uncovering underlying factors or sources in data. This capability is particularly useful in applications such as thermal analysis, where distinct thermal signals corresponding to individual defects need to be isolated and characterized.

The ICA model assumes that the observed data $\mathbf{X} \in \mathbb{R}^{M \times K}$ is a linear mixture of independent source signals $\mathbf{S} \in \mathbb{R}^{L \times K}$:

$$\mathbf{X} = \mathbf{A}\mathbf{S}, \tag{21}$$

where $\mathbf{A} \in \mathbb{R}^{M \times L}$ is the unknown mixing matrix, and $L \leq M$ is the number of independent sources. The goal of ICA is to estimate both the source signals $\mathbf{S}$ and the mixing matrix $\mathbf{A}$ from the observed data $\mathbf{X}$.

Before applying ICA, the data undergoes preprocessing steps, specifically centering and whitening, to simplify the analysis. Centering the data involves subtracting the mean of each variable to ensure that the data has zero mean:

$$\mathbf{X}_{\text{centered}} = \mathbf{X} - \mu, \quad \mu = \frac{1}{K} \sum_{k=1}^{K} \mathbf{x}_k. \tag{22}$$

Whitening the data further decorrelates the variables and scales them to have unit variance:

$$\mathbf{X}_{\text{whitened}} = \mathbf{V}\mathbf{\Lambda}^{-1/2}\mathbf{V}^{\top}\mathbf{X}_{\text{centered}}, \tag{23}$$

where $\mathbf{V}$ and $\mathbf{\Lambda}$ are the eigenvectors and eigenvalues obtained from the eigen decomposition of the covariance matrix $\mathbf{C}$:

$$\mathbf{C} = \mathbf{X}_{\text{centered}}\mathbf{X}_{\text{centered}}^{\top} = \mathbf{V}\mathbf{\Lambda}\mathbf{V}^{\top}. \tag{24}$$

After whitening, the ICA model simplifies to:

$$\mathbf{X}_{\text{whitened}} = \mathbf{W}\mathbf{S}, \tag{25}$$

where $\mathbf{W}$ is the new mixing matrix to be estimated.

The estimation of the independent components $\mathbf{S}$ involves finding an unmixing matrix $\mathbf{W}$ such that the components of $\mathbf{S}$ are as statistically independent as possible. Statistical independence implies that the joint probability distribution of the components factorizes into the product of their individual distributions:

$$p(\mathbf{S}) = \prod_{i=1}^{L} p(s_i). \tag{26}$$

To achieve this, ICA employs contrast functions $\mathcal{F}$ that measure the non-Gaussianity of the components, as independent components tend to be non-Gaussian. Common contrast functions include kurtosis and negentropy:

$$\text{Kurt}(s_i) = \mathbb{E}[s_i^4] - 3(\mathbb{E}[s_i^2])^2, \tag{27}$$

$$J(s_i) = H(s_i^{\text{Gauss}}) - H(s_i), \tag{28}$$

where H denotes entropy and s_i^{Gauss} is a Gaussian variable with the same mean and variance as s_i.

The ICA optimization problem is formally expressed as:

$$\max_{\mathbf{W}} \sum_{i=1}^{L} \mathcal{F}(s_i), \tag{29}$$

subject to the constraint that $\mathbf{W}$ is orthogonal due to the whitening step:

$$\mathbf{W}\mathbf{W}^{\top} = \mathbf{I}. \tag{30}$$

One of the most efficient algorithms for solving this optimization problem is the FastICA algorithm, which iteratively updates the weight matrix $\mathbf{W}$ using a fixed-point iteration scheme. The steps of the FastICA algorithm are as follows:

1. Initialize $\mathbf{W}$ with a random orthogonal matrix.
2. For each row $\mathbf{w}_i$ of $\mathbf{W}$:

$$\mathbf{w}_i^{\text{new}} = \mathbb{E}[\mathbf{X}_{\text{whitened}} g(\mathbf{w}_i^{\top}\mathbf{X}_{\text{whitened}})] - \mathbb{E}[g'(\mathbf{w}_i^{\top}\mathbf{X}_{\text{whitened}})]\mathbf{w}_i, \tag{31}$$

$$\mathbf{w}_i^{\text{new}} = \frac{\mathbf{w}_i^{\text{new}}}{\|\mathbf{w}_i^{\text{new}}\|}. \tag{32}$$

3. Orthogonalize $\mathbf{W}$ using the symmetric decorrelation method:

$$\mathbf{W} \leftarrow \frac{3\mathbf{W} - \mathbf{W}\mathbf{W}^{\top}\mathbf{W}}{2}. \tag{33}$$

4. Check for convergence. If not converged, repeat the update steps.

Here, $g(\cdot)$ is a non-linear function, such as $g(u) = \tanh(u)$, and $g'(\cdot)$ is its derivative. The iterative process continues until the changes in $\mathbf{W}$ fall below a predefined threshold, indicating convergence.

Once the optimal unmixing matrix $\mathbf{W}$ is determined, the independent components $\mathbf{S}$ are extracted as:

$$\mathbf{S} = \mathbf{W}\mathbf{X}_{\text{whitened}}. \tag{34}$$

These independent components represent distinct thermal signals associated with individual defects, enabling their isolation and characterization.

In the context of thermal analysis, ICA extends the capabilities of PCA by not only decorrelating the data but also enforcing statistical independence among the extracted components. This makes ICA a powerful tool for separating mixed thermal signals into their original, independent sources, which is particularly useful for isolating and analyzing distinct thermal events or defects.

3. Results

In the present section the results from PCA and ICA analysis on the experimental acquisition of flying laser spot tests. The data analysis was performed on three datasets corresponding to different scanning speeds: v_1, v_2, and v_3. For each dataset, the following step were performed:

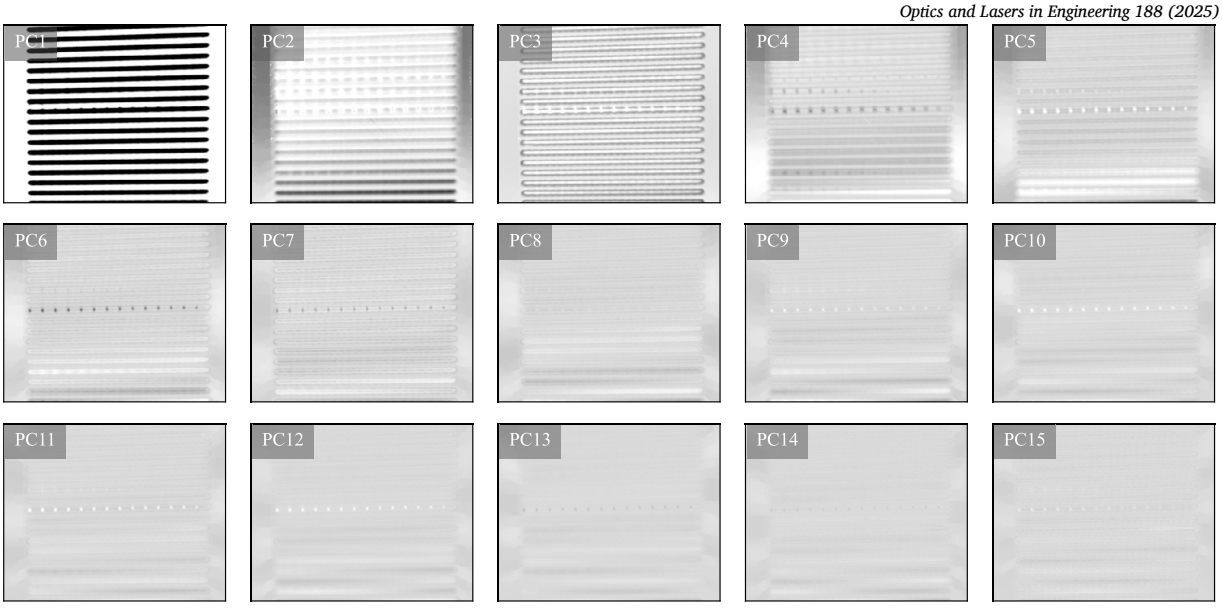

Fig. 4. First three principal components obtained from PCA for the v_1 dataset.

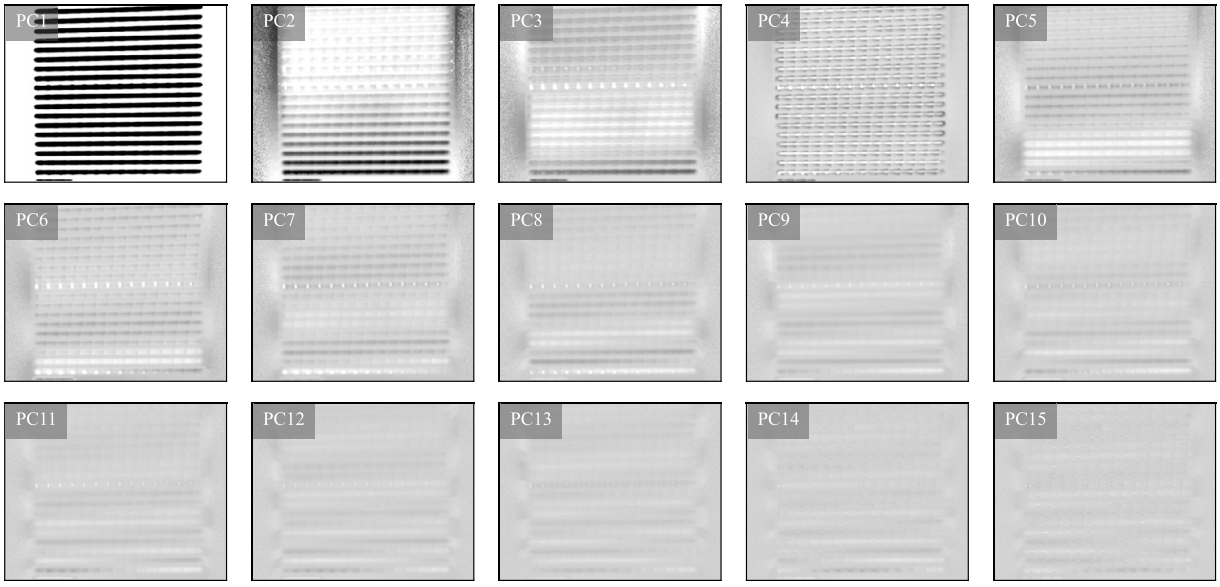

Fig. 5. First three principal components obtained from PCA for the v_2 dataset.

temporal alignment, PCA, and ICA. All the figures are presented in gray-scale colors, where white stand for the minimum value, and black for the maximum.

In the figures the spherical defects cover the lower half of each single image, the notch defects the upper half. The defect depth increases on vertical direction: defects near the surface are lower and deeper defect are upper. While the defect size increases from left to right: defects on the left are larger, while going to the right they became smaller.

3.1. Principal component analysis (PCA)

PCA was systematically applied to the aligned temperature datasets to uncover the principal modes of thermal variation inherent in the data. This transformation facilitates the identification of dominant patterns and structures within the data, which, in this context, correspond to thermal diffusion behaviors associated with embedded defects.

Figs. 4, 5, and 6 illustrate the first three principal components (PC1, PC2, PC3) derived from each respective dataset. The labels PC1, PC2, PC3, etc., denote the sequence of principal components, with PC1 capturing the highest variance, followed by PC2, and so on. These initial components represent the majority of the variance present in the thermal data, thereby highlighting the most significant thermal diffusion patterns linked to the embedded defects.

The first principal component (PC1) consistently reveals the laser scanning path across all three laser scan speeds tested. This component prominently displays the laser track lines as black lines, indicating regions of significant thermal activity corresponding to the laser's movement. Additionally, subtle defect signatures become discernible near the central horizontal line within the background of PC1, suggesting that major thermal variations are strongly influenced by the scanning trajectory.

Delving deeper into the datasets, the analysis conducted at the first laser scan speed (v_1)—as depicted in Fig. 4—shows that principal components PC3 through PC6 effectively capture the nearest notch defects. These notch defects are prominently located near the central horizontal line and are visible across multiple components. Specifically, the sec-

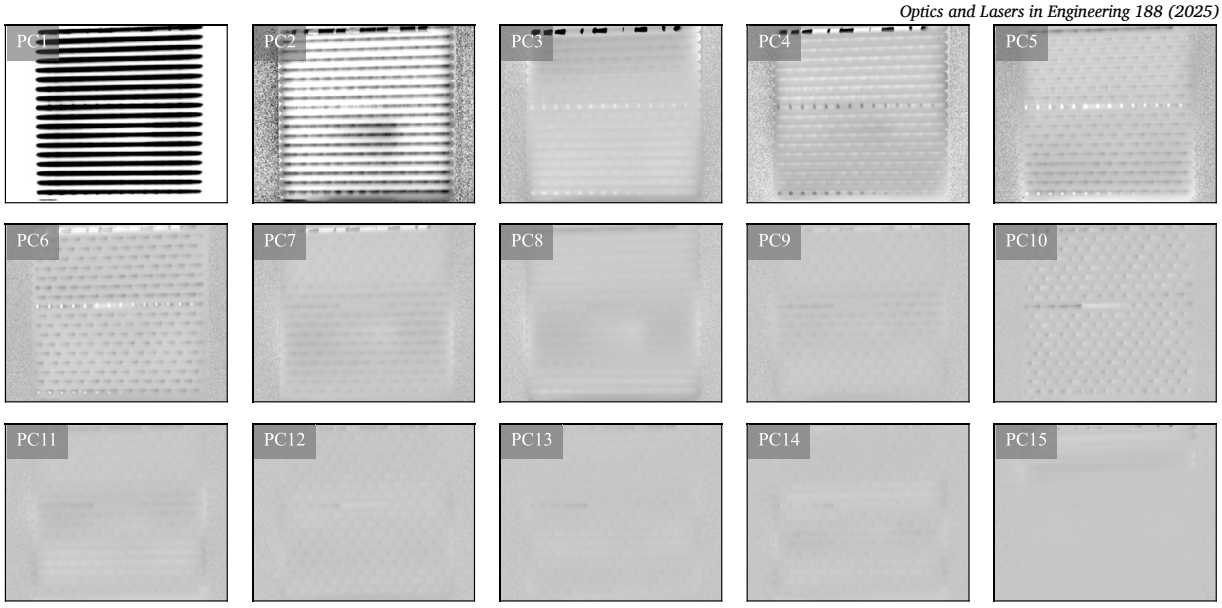

Fig. 6. First three principal components obtained from PCA for the v_3 dataset.

ond line of notch defects is slightly observable up to the first half of the specimen from the left. Beyond this region, an increase in defect depth renders these defects less visible in the higher-order principal components. Importantly, the visibility of notch defects across varying depths underscores the sensitivity of PCA in detecting defects irrespective of their dimension.

In contrast, Figs. 5 and 6 reveal that in the second principal component (PC2), a distinct black shadow appears in the southeast region of the images, slightly below the central horizontal line. This artifact is identified as a reflection of the thermal camera on the specimen's surface. Despite this, the central line of the largest notch defects remains consistently visible across both v_2 and v_3 laser scan speeds, reinforcing the robustness of PCA in highlighting major defect features. Additionally, in some instances, the upper line of near-surface defects and the lower line of the spherical defects exhibit slight visibility, suggesting that while PCA excels at capturing prominent defects, its sensitivity diminishes for deeper or less pronounced anomalies.

A comparative analysis across the three laser scan speeds (v_1, v_2, and v_3) reveals a consistent pattern: PCA effectively identifies and visualizes the defect nearest to the surface. However, the technique exhibits limitations in detecting the smallest and deepest defects, which may be attributed to their minimal thermal signature relative to larger anomalies. Furthermore, the analysis indicates that defect depth has a more substantial influence on PCA's effectiveness than defect size. This observation suggests that while PCA is adept at discerning large-scale thermal variations, its capacity to detect deeper or subtler defects may require supplementary analytical approaches or enhanced data preprocessing techniques.

It is noteworthy that the defect shapes analyzed in this study are exceptionally small when compared to those typically employed in standard calibration blocks for active thermography. The relatively small dimensions of the defects in this work underscore the high sensitivity of the proposed analysis methods. However, the challenge remains in enhancing PCA's capability to reliably capture even smaller defects, potentially through the integration of complementary techniques such as ICA or advanced machine learning algorithms.

PCA proves to be a valuable tool in the analysis of thermal data for defect detection, effectively highlighting major thermal diffusion patterns associated with significant defects. Nonetheless, the limitations observed in detecting deeper defects underscore the necessity for continued methodological advancements to achieve comprehensive defect characterization in high-precision applications.

3.2. Independent component analysis (ICA)

ICA was applied to the aligned temperature datasets with the objective of extracting statistically independent thermal signals. ICA is an advanced computational technique that decomposes multivariate data into additive, statistically independent non-Gaussian components. Unlike PCA, which focuses on uncorrelated components by maximizing variance, ICA seeks to identify components that are not only uncorrelated but also statistically independent, thereby providing a more refined separation of underlying signal sources. This capability is particularly valuable in thermal imaging applications, where distinguishing between overlapping thermal signatures and eliminating noise and artifacts are critical for accurate defect detection and characterization.

Figs. 7, 8, and 9 present independent components derived from each respective dataset obtained at different laser scan speeds. These analyses were conducted in addition to PCA to enhance non-destructive imaging by effectively isolating independent thermal signals and mitigating the influence of noise and imaging artifacts. A preliminary observation across the three tests reveals that the slowest scanning speed (v_1) yields superior image quality compared to the faster scanning speeds (v_2 and v_3). This improvement can be attributed to the increased heat input associated with slower scanning speeds, which enhances thermal contrast and facilitates the more accurate detection of defects.

In the dataset corresponding to the slowest scanning speed (v_1), defects are prominently visible in multiple independent components, specifically IC3, IC5, IC6, IC7, IC8, IC9, IC11, IC12, IC14, and IC15. Among these, IC8 provides the highest contrast, revealing almost three distinct lines of notched defects. The enhanced visibility in IC8 indicates that this component effectively isolates the thermal signatures of the notched defects from other overlapping thermal signals and background noise. Notably, spherical defects do not appear in these components, suggesting that ICA is more sensitive to the thermal variations associated with notched defects under these scanning conditions.

For the medium scanning speed (v_2), many independent components exhibit significant noise and artifacts, which can obscure the underlying thermal signals. However, defects remain distinguishable in IC2, IC5, IC6, IC7, IC8, IC9, IC10, IC11, IC12, IC13, IC14, and IC15. Consistently, the central line corresponding to the notch defects near to the surface is prominently visible across these components. Additionally, in certain components such as IC7, IC10, IC11, and IC13, the lower line of defects—associated with the nearest spherical defects—begins to emerge. This partial visibility indicates that while ICA maintains

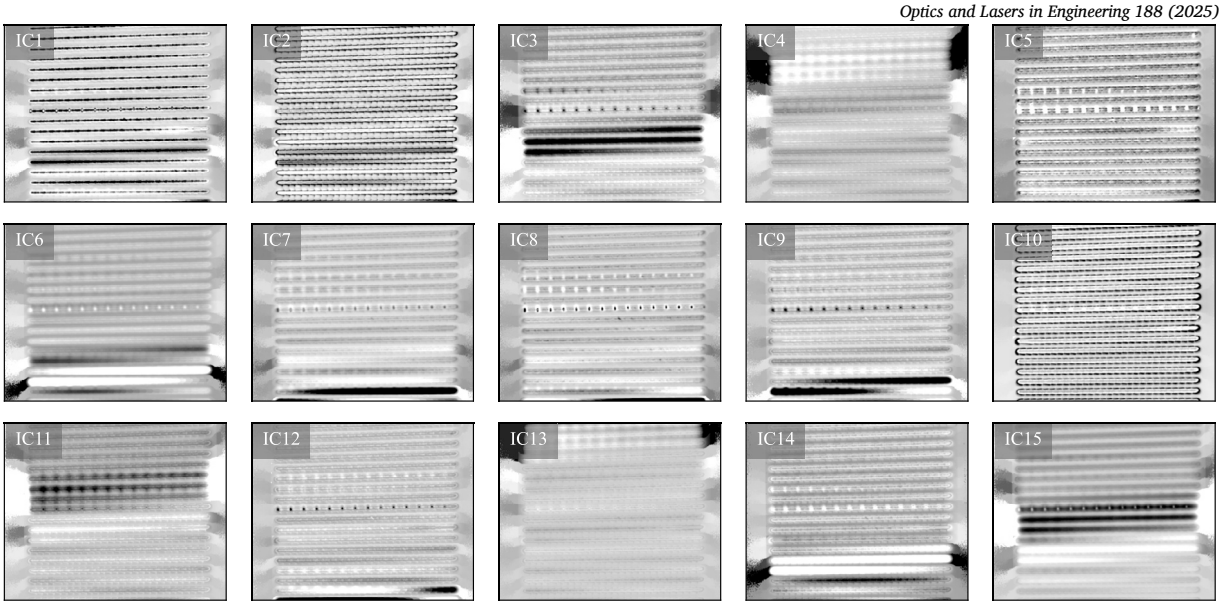

Fig. 7. First three independent components derived from ICA for the v_1 dataset. These components isolate distinct thermal signatures associated with specific defects.

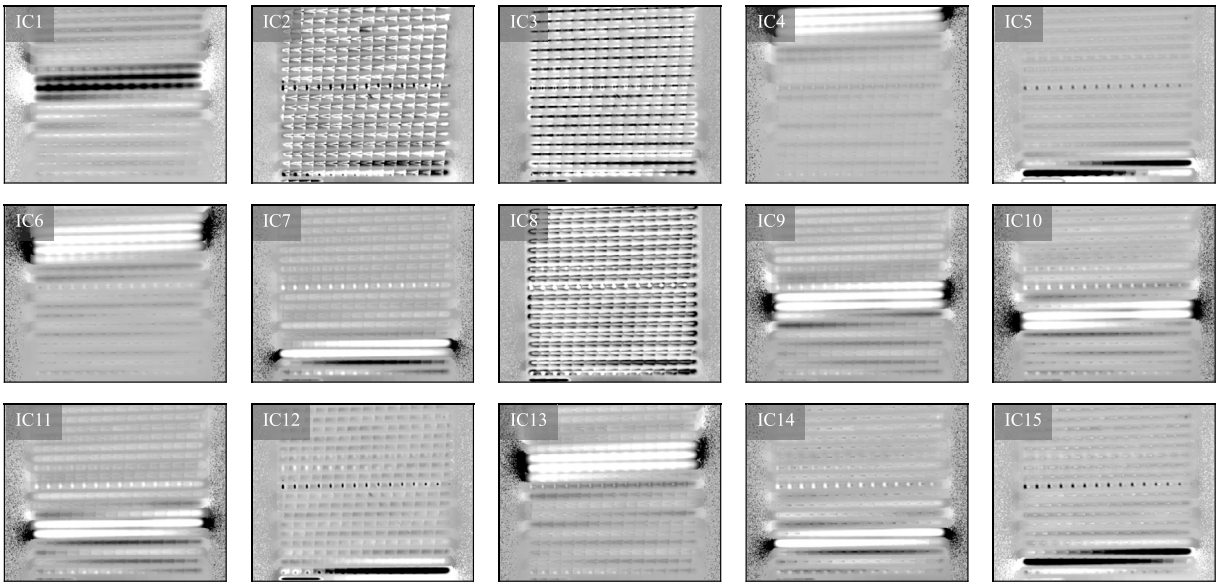

Fig. 8. First three independent components derived from ICA for the v_2 dataset.

effectiveness in isolating major defects, the increased scanning speed introduces complexities that affect the clarity of smaller or deeper defects.

At the highest scanning speed (v_3), the central line of defects remains clearly visible across various independent components. Specifically, IC8, IC9, IC10, and IC13 reveal the nearest spherical defects. The consistency of defect visibility in these components underscores ICA's robustness in extracting significant thermal signals even under challenging scanning conditions. However, similar to the v_2 dataset, some components may still be affected by residual noise and artifacts, which can limit the detection of smaller or deeper defects.

The comparative analysis across the three laser scan speeds (v_1, v_2, and v_3) demonstrates that ICA effectively enhances the quality of thermal imaging with respect to PCA by isolating independent thermal signals corresponding to defects.

The slowest scanning speed (v_1) consistently produces the best results, characterized by clearer defect visualization and higher contrast in the independent components. This performance advantage is primarily due to the higher heat input at slower scanning speeds, which amplifies the thermal signatures of defects and improves the overall thermal contrast in the images. In contrast, faster scanning speeds (v_2 and v_3) result in increased noise and artifacts within the independent components.

Despite this, ICA remains capable of isolating significant defect-related signals, although the clarity and contrast are somewhat reduced compared to the v_1 dataset. This observation highlights the trade-off between scanning speed and image quality, emphasizing the importance of optimizing scanning parameters to balance data acquisition efficiency with defect detection accuracy.

The analysis reveals that notch-shaped defects are more prominently detected than spherical defects across all scanning speeds. This difference can be attributed to the inherent differences in thermal diffusion patterns associated with these defect shapes. Notched defects, with their irregular geometries, disrupt thermal diffusion more significantly, creating pronounced thermal gradients that are more readily captured by ICA.

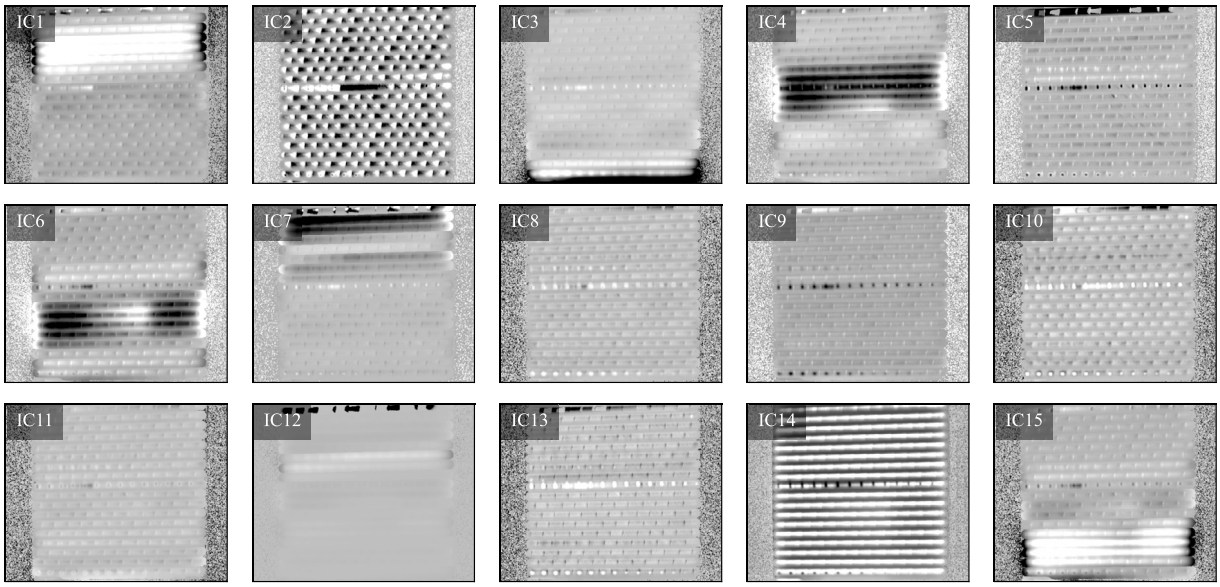

Fig. 9. First three independent components derived from ICA for the v_3 dataset.

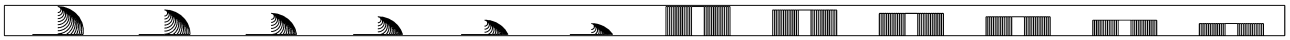

Fig. 10. Visualization of differences in depth of spherical and flat-top notches.

The flat tops of notches (see Fig. 10) act as thermal barriers, interrupting heat flow and generating distinct thermal signatures that enhance defect visibility. Conversely, spherical defects exhibit a more uniform distribution of thermal flux around their surfaces, resulting in subtler thermal gradients that are less conspicuous in the independent components.

The symmetric geometry of spherical defects (see Fig. 10) allows for more efficient heat distribution, thereby reducing the thermal contrast relative to notched defects. Consequently, while ICA effectively detects large spherical defects, its sensitivity to smaller or less pronounced spherical anomalies is limited.

The study successfully detected spherical defects with a diameter from 4 mm to 0.8 mm across depths ranging from 0.2 mm to 1 mm. For notched defects, detection was achieved for notches with a constant width of 2 mm and lengths varying from 2 mm to 10 mm, with depths spanning from 0.2 mm to 2 mm for longer notches and up to 1.5 mm for shorter notches. These detection thresholds underscore ICA's capability in identifying defects of varying geometries and sizes. However, the detection of smaller or shallower defects remains challenging, particularly under higher scanning speeds where thermal signatures are less pronounced.

The primary outcome of applying ICA to the thermal data is the validation of flying spot thermography as a viable method for reconstructing signals akin to those obtained from pulsed thermography. By leveraging laser scanning and subsequent signal analysis through PCA and ICA, it is possible to enhance non-destructive imaging techniques, achieving clearer defect visualization and more accurate defect characterization. The superior performance of ICA in providing better contrast imaging, especially at the slowest scanning speed (v_1), highlights its potential as a powerful tool in non-destructive testing applications. While both PCA and ICA contribute to the enhancement of thermal imaging, ICA demonstrates a distinct advantage in isolating independent thermal signals and improving image contrast. PCA effectively reduces data dimensionality and highlights major thermal variations, but ICA complements this by further decomposing the data into statistically independent components, thereby enhancing defect visibility and reducing the impact of noise and artifacts.

4. Conclusion

The study successfully demonstrated the application of Principal Component Analysis (PCA) and Independent Component Analysis (ICA) to aligned temperature datasets obtained from flying spot laser thermography for non-destructive defect detection in plastic materials.

One of the main outcomes is that flying spot laser thermography can be used to reconstruct a signal similar to that obtained with lamp pulsed thermography, thereby enabling the application of standard data analysis methods. This approach is particularly useful when large heat inputs are required or when scanning large areas, as traditional lamp thermography would require prolonged exposure times and suffers from power loss over distance.

It was demonstrated that PCA effectively reduced the dimensionality of the thermal data, identifying the principal modes of thermal variation and highlighting the most significant thermal diffusion patterns associated with embedded defects. The analysis revealed that PCA is adept at visualizing large-scale defects, particularly notched anomalies, by capturing the majority of the variance in the thermal signals. However, PCA exhibited limitations in detecting smaller or less pronounced defects, primarily due to their minimal thermal signatures relative to larger anomalies.

The comparative analysis across different laser scan speeds underscored the importance of optimizing scanning parameters to balance data acquisition efficiency with defect detection accuracy. Slower scanning speeds (v_1) consistently yielded superior image quality, facilitating the accurate detection of both notched and spherical defects. In contrast, faster scanning speeds introduced increased noise and artifacts, which, although partially mitigated by ICA, still posed challenges in identifying smaller or deeper defects. Overall, ICA analysis at the slowest speed, v_1, showed the best results.

Despite the successes, the study acknowledged the inherent limitations of both PCA and ICA in detecting the smallest defects, highlighting the need for methodological advancements to achieve comprehensive defect characterization. In future work, simulation-based optimization of scanning parameters and the integration of advanced machine learning algorithms (such as deep neural networks) will be explored to further improve defect detection, particularly for small and shallow defects.

Additionally, the potential application of the method to cylindrical specimens has been identified as a promising direction for further research.

CRediT authorship contribution statement

Luca Santoro: Writing – original draft, Visualization, Supervision, Software, Methodology, Investigation, Data curation, Conceptualization. **Raffaella Sesana:** Writing – review & editing, Validation, Supervision, Resources.

Declaration of competing interest

The authors declare that they have no known competing financial interests or personal relationships that could have appeared to influence the work reported in this paper.

Data availability

All the algorithms used in this paper are part of the `atpp` Python library, developed by the authors, and available at the link: https://github.com/lucasantoro97/atpp. Documentation is available at https://lucasantoro97.github.io/atpp/. Feel free to contact the authors for any questions on the code at luca.santoro@polito.it.

References

[1] Ahmad J, Akula A, Mulaveesala R, Sardana H. Barker-coded thermal wave imaging for non-destructive testing and evaluation of steel material. IEEE Sens J 2019;19:735–42.
[2] Ahmad J, Akula A, Mulaveesala R, Sardana H. Probability of detecting the deep defects in steel sample using frequency modulated independent component thermography. IEEE Sens J 2021;21:11244–52.
[3] Quercio M, Santoro L, Poskovic E, Sesana R, Canova A. Magnetic and thermal characterization of fe2.9wt.%si for magnetic shielding applications. IEEE Access 2024:1.
[4] Santoro L, Quercio M, Canova A, Sesana R. Measuring thermal and electrical performances of additively manufactured magnetic shielding material: an active thermography approach. Nondestruct Test Eval 2024:1–24.
[5] Borghese V, Santoro L, Santini S, Sesana R. Correlation between thermal and density properties of chestnuts: preliminary results of experimental non-destructive testing. Arch Civ Mech Eng 2024;24:1–15.
[6] Santoro L, Sesana R, Diller J, Radlbeck C, Mensinger M. Dissipative and thermal aspects in cyclic loading of additive manufactured aisi 316l. Eng Fail Anal 2024;163:108446.
[7] Dell'Avvocato G, Palumbo D. Thermographic procedure for the assessment of Resistance Projection Welds (RPW): investigating parameters and mechanical performances. J Adv Join Process 2024;9:100177.
[8] Dell'Avvocato G, Palumbo D, Pepe R, Galietti U. Non-destructive evaluation of resistance projection welded joints (RPW) by flash thermography. IOP Conf Ser, Mater Sci Eng 2021;1038:012003.
[9] Dell'Avvocato G, Palumbo D, Palmieri ME, Galietti U. Non-destructive thermographic method for the assessment of heat treatment in boron steel. In: SPIE; 2022. p. 8.
[10] Dell'Avvocato G, Palumbo D, Galietti U. A non-destructive thermographic procedure for the evaluation of heat treatment in Usibor®1500 through the thermal diffusivity measurement. NDT E Int 2023;133.
[11] Ahmed J, Baloch GA, Tian GY. Wavelet domain based defect detection using optical thermography. ACM international conference proceeding series; 2019. p. 83–7.
[12] Ba A, Yi Q, Zhu J, Bui H-K, Tian GY, Berthiau G, et al. Impact damages detection on cfrp using eddy current pulsed thermography. Studies in applied electromagnetics and mechanics, vol. 45. 2020. p. 147–51.
[13] Quercio M, Povskovic E, Franchini F, Fracchia E, Ferraris L, Canova A, et al. Application of active thermography for the study of losses in components produced by laser powder bed fusion. J Magn Magn Mater 2024.
[14] Matarrese T, Palumbo D, Galietti U. Comparison in the transient regime of four lock-in thermography algorithms by means of synthetic and experimental data on CFRP. NDT E Int 2023;139:102925.
[15] Bai L, Gao B, Tian S, Cheng Y, Chen Y, Tian GY, et al. A comparative study of principal component analysis and independent component analysis in eddy current pulsed thermography data processing. Rev Sci Instrum 2013;84.
[16] Bai L, Liang Y, Shao J, Cheng Y, Zhou Q, Zhang J. Moran's index-based tensor decomposition for eddy current pulsed thermography sequence processing. IEEE Trans Instrum Meas 2021;70.
[17] Santoro L, Razza V, Maddis MD. Frequency-based analysis of active laser thermography for spot weld quality assessment. Int J Adv Manuf Technol 2024;130:3017–29.
[18] Sesana R, Santoro L, Curà F, Nardo RM, Pagano P. Assessing thermal properties of multipass weld beads using active thermography: microstructural variations and anisotropy analysis. Int J Adv Manuf Technol 2023;128:2525–36.
[19] Santoro L, Sesana R, Nardo RM, Curá F. Infrared in-line monitoring of flaws in steel welded joints: a preliminary approach with smaw and gmaw processes. Int J Adv Manuf Technol 2023;128:2655–70.
[20] Chen K, Bai L, Chen Y, Cheng Y, Tian S, Zhu P. Defect automatic identification of eddy current pulsed thermography. J Sens 2014:2014.
[21] Chen H, Zhang Z, Yin W, Zhou G, Wang L, Li Y, et al. Shape characterization and depth recognition of metal cracks based on laser infrared thermography and machine learning. Expert Syst Appl 2024;238.
[22] Ebrahimi S, Fleuret JR, Klein M, Théroux L-D, Ibarra-Castanedo C, Maldague XPV. Data enhancement via low-rank matrix reconstruction in pulsed thermography for carbon-fibre-reinforced polymers. Sensors 2021;21.
[23] Fernandes HC, Zhang H, Morioka K, Ibarra-Castanedo C, López F, Maldague XPV, et al. Infrared thermography for cfrp inspection: computational model and experimental results. Proceedings of SPIE - the international society for optical engineering, vol. 9861. 2016.
[24] Gavrilov D, Maev RG. Extraction of independent structural images for principal component thermography. Appl Sci (Switzerland) 2018;8.
[25] Halloua H, Elhassnaoui A, Saifi A, Elamiri A, Obbadi A, Errami Y, et al. Neural networks and genetic algorithms for the evaluation of coatings thicknesses in thermal barriers by infrared thermography data. Procedia Struct Integr 2017;5:997–1004.
[26] Halloua H, Elhassnaoui A, Zrhaiba A, Kraibaa S, Obbadi A, Errami Y, et al. Defects depth estimation in a cfrp material by active infrared thermography using neural network. J Optoelectron Adv Mater 2020;20:156–62.
[27] He Y, Yang R, Wu X, Huang S. Dynamic scanning electromagnetic infrared thermographic analysis based on blind source separation for industrial metallic damage evaluation. IEEE Trans Ind Inform 2018;14:5610–9.
[28] D'Accardi E, Finis RD, Dell'Avvocato G, Masciopinto G, Palumbo D, Galietti U. Conduction thermography for non-destructive assessment of fatigue cracks in metallic materials. Infrared Phys Technol 2024;140:105394.
[29] D'Accardi E, Dell'Avvocato G, Masciopinto G, Marinelli G, Fumarola G, Palumbo D, et al. Evaluation of typical rail defects by induction thermography: experimental results and procedure for data analysis during high-speed laboratory testing. Quant InfraRed Thermogr J 2024.
[30] He Z, Wang H, He Y, Zhang G, Wang J, Zou G, et al. Joint scanning laser thermography defect detection method for carbon fiber reinforced polymer. IEEE Sens J 2020;20:328–36.
[31] He Z, Wang H, Li Y, Zhang Z, Zhang Y, Bi H, et al. A deconvolutional reconstruction method based on Lucy-Richardson algorithm for joint scanning laser thermography. IEEE Trans Instrum Meas 2021;70.
[32] Joubert P-Y, Hermosilla-Lara S, Placko D, Lepoutre F, Piriou M. Enhancement of open-crack detection in flying-spot photothermal non-destructive testing using physical effect identification. Quant InfraRed Thermogr J 2006;3:53–70.
[33] Kaur K, Sharma A, Rani A, Kher V, Mulaveesala R. Physical insights into principal component thermography. Insight, Non-Destr Test Cond Monit 2020;62:277–91.
[34] Lei L, Ferrarini G, Bortolin A, Cadelano G, Bison P, Maldague X. Liquid nitrogen cooling in ir thermography applied to steel specimen. Proceedings of SPIE - the international society for optical engineering, vol. 10214. 2017.
[35] Li Z, Guo X. Factor analysis used in pulsed infrared thermographic ndt. Beijing Hangkong Hangtian Daxue Xuebao/J Beijing Univ Aeronaut Astronaut 2010;36:622–6.
[36] Liu H, Li G, Zhao Y. A sliding-window principal component thermography reconstruction approach for enhancement and identification of electronic components internal structure. Measurement, J Int Meas Confed 2021;184.
[37] Luo Z, Wang H, Huang Y, Shen P, Zheng E, Zhang H. Nondestructive detection of cfrp subsurface defects using transient lock-in thermography. J Therm Anal Calorim 2024.
[38] Milovanović B, Pečur I Banjad, Štirmer N. The methodology for defect quantification in concrete using ir thermography. J Civ Eng Manag 2017;23:573–82.
[39] Nategh K, Farahani M. Defect detection in thermography non-destructive testing by means of signal processing and k-means clustering. Nondestruct Test Eval 2024.
[40] Pasha MM, Rao G Subba, Suresh B, Tabassum S. Inspection of defects in cfrp based on principal components. Int J Recent Technol Eng 2019;8:2367–70.
[41] Pereira Barella B, Rosa R Garcia, Barbosa de Oliveira G Maira, Fernandes H. Enhancing fault characterisation in composites using infrared thermography: a bee colony optimisation approach with self-organising maps. Quant InfraRed Thermogr J 2024.
[42] Rodríguez-Martin M, Pisonero J, González-Aguilera D, Madruga FJ. Flash thermography to detect and evaluate impacts in polycarbonate parts produced by additive manufacturing. NDT E Int 2024;146.
[43] Sels S, Bogaerts B, Verspeek S, Ribbens B, Steenackers G, Penne R, et al. 3d defect detection using weighted principal component thermography. Opt Lasers Eng 2020;128.
[44] Shrestha R, Kim W. Non-destructive testing and evaluation of materials using active thermography and enhancement of signal to noise ratio through data fusion. Infrared Phys Technol 2018;94:78–84.
[45] Suresh B, Sekhar B Raja. Detecting delaminations in cfrp using quadratic frequency modulated thermal wave imaging. Lecture notes in mechanical engineering; 2024. p. 237–46.

[46] Theodorakeas P, Avdelidis N, Ibarra-Castanedo C, Koui M, Maldague X. Pulsed thermographic inspection of cfrp structures: experimental results and image analysis tools. Proceedings of SPIE - the international society for optical engineering, vol. 9062. 2014.

[47] Tian L, Wang Z, Liu W, Cheng Y, Alsaadi FE, Liu X. A new gan-based approach to data augmentation and image segmentation for crack detection in thermal imaging tests. Cogn Comput 2021;13:1263–73.

[48] Tong Z, Xie S, Chen H-e, Qiu J, Cai W, Pei C, et al. Quantitative mapping of depth profile of fatigue cracks using eddy current pulsed thermography assisted by pca and 2d wavelet transformation. Mech Syst Signal Process 2022;175.

[49] Triska V, Hnidka J, Nova B, Hajda S, Kubecek P. Active thermography inspection of water ingress into the sandwich structure of an helicopter blade. In: 2023 9th international conference on military technologies, ICMT 2023 - proceedings; 2023.

[50] Laudani A, Corti F, Intravaia M, Lozito GM, Quercio M, Fulginei FR. Monitoring of bipv by means of a low cost wireless sensor network. In: 2024 IEEE international conference on environment and electrical engineering and 2024 IEEE industrial and commercial power systems Europe (EEEIC / I&CPS Europe); 2024. p. 01–5.

[51] Wang Y, Ke H, Shi J, Gao B, Tian G. Impact damage detection and characterization using eddy current pulsed thermography. In: Proceedings of 2016 IEEE far East NDT new technology and application forum, FENDT 2016; 2017. p. 223–6.

[52] Wei J, Wang F, Liu J, Wang Y, He L. A laser arrays scan thermography (lasst) for the rapid inspection of cfrp composite with subsurface defects. Compos Struct 2019;226.

[53] Wei Y, Ye Y, He H, Su Z, Ding L, Zhang D. Multi-frequency fused lock-in thermography in detecting defects at different depths. J Nondestruct Eval 2022;41.

[54] Wu J-Y, Sfarra S, Yao Y. Sparse principal component thermography for subsurface defect detection in composite products. IEEE Trans Ind Inform 2018;14:5594–600.

[55] Xiong Z, Bai L, Liang Y, Tian L, Chen C, Cheng Y. Total variation regularized sparse tensor decomposition for eddy current pulsed thermography sequence processing, conference record. In: IEEE instrumentation and measurement technology conference 2023-May; 2023.

[56] Xu C, Gong X, Zhang W, Chen G. An investigation on eddy current pulsed thermography to detect surface cracks on the tungsten carbide matrix of polycrystalline diamond compact bit. Appl Sci (Switzerland) 2017;7.

[57] Xu C, Xie J, Wu C, Gao L, Chen G, Song G. Enhancing the visibility of delamination during pulsed thermography of carbon fiber-reinforced plates using a stacked autoencoder. Sensors (Switzerland) 2018;18.

[58] Yan Z, Chen C-Y, Luo L, Yao Y. Stable principal component pursuit-based thermographic data analysis for defect detection in polymer composites. J Process Control 2017;49:36–44.

[59] Yang J, Dong L, Wang H, Xing Z, Di Y, Gao C, et al. The curve cluster analyses for the characterizations of material defects by long-pulsed laser thermography. Infrared Phys Technol 2022;120.

[60] Yao Y, Sfarra S, Lagüela S, Ibarra-Castanedo C, Wu J-Y, Maldague XP, et al. Active thermography testing and data analysis for the state of conservation of panel paintings. Int J Therm Sci 2018;126:143–51.

[61] Yi Q, Tian G, Malekmohammadi H, Zhu J, Laureti S, Ricci M. New features for delamination depth evaluation in carbon fiber reinforced plastic materials using eddy current pulse-compression thermography. NDT E Int 2019;102:264–73.

[62] Zhang H, Sfarra S, Osman A, Sarasini F, Netzelmann U, Valeske B, et al. Nondestructive evaluation of low-velocity impact-induced damage in basalt-carbon hybrid composite laminates using eddy current-pulsed thermography. Opt Eng 2019;58.

[63] Zhang Y, Xu C, Liu P, Xie J, Han Y, Liu R, et al. One-dimensional deep convolutional autoencoder active infrared thermography: enhanced visualization of internal defects in frp composites. Composites, Part B, Eng 2024;272.

[64] Zhou Y, Liu J, Zhou X, Feng L, Chen L, Liu Z. Optical flow amplitude-based method for detection and quantitative evaluation of impact damage in cfrp. IEEE Trans Instrum Meas 2024;73.

[65] Zhu P, Bai L, Cheng Y, Yin C. Selection of significant independent components in eddy current pulsed thermography non-destructive testing. In: Conference record - IEEE instrumentation and measurement technology conference 2015-July; 2015. p. 853–7.

[66] Zhu J, Wang Z, Tian G. Comparative study of eddy current pulsed and long pulse optical thermography for defect detection in aluminium plate. In: ICAC 2018 - 2018 24th IEEE international conference on automation and computing: improving productivity through automation and computing; 2018.

[67] Zhu J, Tiany G, Min Q, Wu J. Comparison study of different features for pocket length quantification of angular defects using eddy current pulsed thermography. IEEE Trans Instrum Meas 2019;68:1373–81.

[68] Zhu P, Cheng Y, Bai L, Tian L. Local sparseness and image fusion for defect inspection in eddy current pulsed thermography. IEEE Sens J 2019;19:1471–7.

[69] Zhu P, Tian L, Cheng Y. Improvement of defect feature extraction in eddy current pulsed thermography. IEEE Access 2019;7:48288–94.

Luca Santoro is a dedicated researcher at the Politecnico di Torino, within the Department of Mechanical and Aerospace Engineering. His expertise lies in non-destructive testing techniques and the mechanical fatigue of materials. He specializes in active thermography and innovative ultrasonic applications, with a recent focus on using thermography for monitoring welding processes. His work has led to significant industrial applications and the development of patents, contributing to advancements in material testing and engineering practices.

Raffaella Sesana is M.Sc. in Mechanical Engineering, Ph.D. in Machine Design. Today Associate Professor in Department of Mechanic and Aerospace Engineering, Politecnico di Torino. The main research topics are HCF, non-destructive fatigue limit and damage assessment, LCF and TMF damage models, characterization of materials and components, constitutive models for cyclic plastic behavior of metallic, polymeric materials, foams, thermographic NDT.